On the identification of deeper defect levels in organic photovoltaic devices

John A. Carr[1] and Sumit Chaudhary[1,2,a)]
[1]*Department of Electrical and Computer Engineering, Iowa State University, Ames, Iowa 50011, USA*
[2]*Department of Materials Science Engineering, Iowa State University, Ames, Iowa 50011, USA*

Defect levels play a significant role in altering organic photovoltaic (OPV) performance, affecting device aspects such as recombination, carrier transport, and Fermi-level pinning. In the ongoing effort to optimize the promising OPV technology, the identification, characterization, and potential mitigation or enhancement of such defect states remain important regions of interest. Herein, low frequency admittance spectroscopy is coupled with a high frequency, point-by-point capacitance versus voltage measurement to reveal a previously unknown deep-defect distribution in poly (3-hexylthiophene) based OPVs. The capacitance models of Cohen and Lang, Walter *et al.* and Kimmerling are employed alongside a trap-free dark current model to give good characterization and substantiation to the discovered band. Repetitions of the measurements on devices with and without a fullerene acceptor show the measured distribution to contain acceptor-like traps spatially located in the polymer bulk. The findings presented here are important for the understanding and optimization of organic solar cells and we expect the presented methods to be generally applicable to other OPV material sets. © 2013 AIP Publishing LLC. [http://dx.doi.org/10.1063/1.4818324]

I. INTRODUCTION

Organic photovoltaic (OPV) devices have progressed impressively over the last several years. As of late, the power conversion efficiency (PCE) of single junction OPVs is rapidly approaching 10%,[1] with commercialized tandem structures reaching 12%. However, with the Shockley-Queisser (SQ) limit for single-junction cells calculated at around 23%, much scope is left for further improvement.[2] Excess recombination, low carrier mobility, and inadequate exciton diffusion have been cited among the top deficiencies plaguing these devices,[2] highlighting the need for works which study the underlying physical characteristics affecting such parameters.

One such physical characteristic is band-gap residing trap levels, which are known to stem from both intrinsic and extrinsic defects that are seemingly inherent to the OPV system. Such defect bands can significantly affect the abovementioned parameters, introducing charged trap sites, Shockley-Read-Hall (SHR) centers, or both. The former is known to alter the internal electronic landscape, diminishing carrier mobility and reducing the exciton diffusion length;[3–5] while the latter plays an important role in free-carrier loss, especially if the defect exists near a domain interface.[6–9] Further, deep trap states are known to pin the Fermi-level deep within the energy gap,[10] potentially suppressing the achievable open circuit voltage.[11] On the contrary, some defects in OPV devices may be beneficial to the above parameters, giving the system a favorable apparent doping. This doping is known to be advantageous for electrical conductivity as well as the donor-acceptor interfacial electric field.[5,12] Thus, the identification, characterization, and potential mitigation or enhancement of these defect levels remain important areas of interest.

To date, some work has profiled band-gap residing states in poly(3-hexylthiophene) (P3HT), a conjugated polymer commonly employed in OPV devices. Sub-gap optical absorption has identified the molecular orbitals to be Gaussian in nature, broadening of which introduces a distribution of shallower tail-states that lead into deeper, localized levels.[13] Thermally stimulated current (TSC),[14–16] fractional thermally stimulated current (FTSC),[17] capacitance-voltage (CV)[18] and drive-level transient spectroscopy (DLTS)[19] measurements have further elucidated the shallower levels, giving good characterization to this energy regime. Above the Fermi-level, deep-defects have been identified and characterized through photoemission spectroscopy,[20] capacitance-frequency (CF),[21,22] conduction modeling,[23] and (F)TSC measurements.[14,17] However, no report has profiled *deeper* towards the mid-gap, an energy regime which we expect to house a distribution of trap levels.

Herein, using CF, CV, and trap-free dark-current modeling, we report the presence of deeper defects in P3HT:Phenyl-C_{61}-butyric acid methyl ester (PCBM) OPVs. The main band is revealed by low frequency (<1 Hz) CF, which is analyzed using the model of Cohen and Lang as well as that of Walter *et al.*[24,25] This band is then confirmed by a point-by-point differential of high frequency CV, which in turn indicates a uniform doping profile. The total traps discovered via capacitance are well correlated to the total traps measured by dark current modeling, substantiating the measurements and assumptions. Lastly, a comparison of P3HT:PCBM based devices to pure P3HT diodes with two different cathode interfaces shows the traps measured here are likely inherent to the polymer bulk.

II. BACKGROUND, THEORY, AND MOTIVATION

The CV and CF measurements employed in this work exploit the depletion region of a semiconductor junction,

a)Author to whom correspondence should be addressed. Electronic mail: sumitc@iastate.edu. Telephone: 515.294.0606. Present address: 2124 Coover Hall, Ames, Iowa 50011-3060, USA.

which displays a parallel-plate-like capacitance. Consider a pure, crystalline metal/*p*-semiconductor Schottky-interface. The depletion approximation holds and the space charge region acts as a dielectric. Charges at the edge of the region can respond to an alternating current (AC) of suitable frequency and contribute to the depletion capacitance, $C_d = \varepsilon_s A / W_d$.[26] Inserting the classic equation for the depletion width (W_d)[26] and linearizing yields the well-known Mott-Schottky (MS) relation,

$$\frac{1}{C^2} = \frac{2}{A^2 q \epsilon_s N} (V_{bi} - V_{app}), \qquad (1)$$

where ϵ_s is the semiconductor permittivity, A the junction area, V_{bi} the built-in voltage, V_{app} the applied voltage, q the elementary charge, and N the density of mobile-charges. A plot of $1/C^2$ versus V_{app} yields a straight line, from which N and V_{bi} are extracted.

A slightly more complex CV analysis solves Gauss's law for the charge at the depletion edge to reveal the classic *profiler* equation,

$$N(x) = \frac{C^3}{q\epsilon_s A^2} \frac{dV}{dC}, \qquad (2)$$

where x is the spatial depth from the junction ($x = \epsilon_s A / C$).[10] This point-by-point differential ascertains N as a function of film depth. For crystalline materials, the interpretation of the measured N in Eqs. (1) and (2) is straightforward, $N = N_A^- = p$. However, for non-crystalline or otherwise impure semiconductors—such as OPV materials—the interpretation becomes convoluted as bandgap residing defects can also contribute to the depletion capacitance. In such a case, the depletion approximation can breakdown and the capacitance is better defined by $C_d = \varepsilon_s A / \langle x \rangle$, where $\langle x \rangle$ is the first moment of charge response.[10]

Fig. 1(a), which depicts the MS relation of a model OPV device for different AC frequencies, shows an example of such a case. In P3HT based cells, the polymer becomes *p*-doped with exposure to oxygen or moisture[12,27] and creates a Schottky-junction at the cathode,[18,28,29] allowing for capacitance measurements to be leveraged. A strong dependence on both frequency and direct current (DC) bias is seen (Fig. 1(a)). In the low forward/reverse bias region, an increase in the MS slope with increasing frequency is clearly present. This highlights the capacitive response of defect states as a function of the small-signal oscillation. The thermal emission rate of a trap state in a *p*-type semiconductor is quantified by,

$$\frac{1}{\tau_p} = e_p = N_V v_{th} \sigma_p \exp\left(\frac{-E_A}{k_B T}\right), \qquad (3)$$

where N_V is the valence band density of states, v_{th} the thermal velocity, σ_p the capture cross-section, E_A the trap activation energy, T the temperature, and k_B the Boltzmann constant.[10,24,30] Neglecting any temperature dependence, $N_V \nu_{th} \sigma_p$ then defines the attempt-to-escape frequency ($\nu_0 = \omega_0/2\pi$)[25] and the small-signal measurement inherently includes [or excludes] trap states as per the AC frequency.
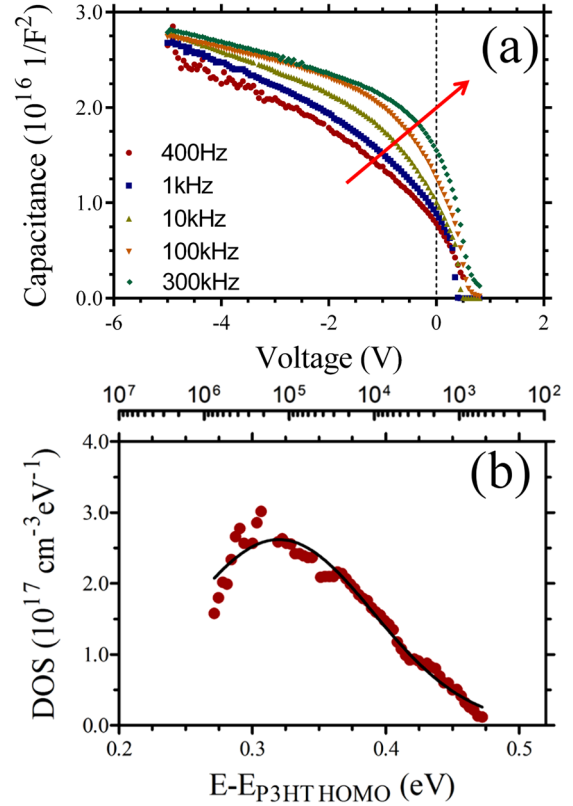

FIG. 1. (a) Mott-Schottky form of CV measurements on P3HT:PCBM BHJ cell. The arrow indicates increasing frequency. (b) Admittance spectroscopy showing deep-defect Gaussian. E_ν is shown on bottom x-axis and frequency (Hz) on top.

This dynamic response is commonly explained in terms of a spatial abscissa, where a distance from the junction interface, x_ω, is defined as per the applied frequency where $\omega\tau_p = 1$.[24,31] Traps crossing the quasiFermi-level further from the junction (with $\omega\tau_p \leq 1$) can change their state and contribute to the depletion capacitance, while those closer cannot. Assuming a constant trap density of states (tDOS), the formalism of Cohen and Lang and work of Mencaraglia *et al.* then shows the depletion capacitance to be defined by $C_d = \varepsilon A/(x_\omega + L_D)$, where L_D is the Debye length.[24,32] The Debye length is defined by

$$L_D = \left[\frac{\varepsilon_s}{q^2 N_T(E_{F0})}\right]^{\frac{1}{2}}, \qquad (4)$$

which is further related to the CF measurement through

$$\left[\frac{d(\varepsilon_s A / C)}{d(\ln \omega)}\right]^{-1} = \frac{1}{L_D}(\ln \omega_{TO} - \ln \omega), \qquad (5)$$

where ω is the applied angular frequency and ω_{TO} the turn on angular frequency.[32,33] Thus, an estimation of the tDOS [among other parameters] is readily obtained.

Similarly, the AC response of trap states is commonly explained in terms of a demarcation energy, defined by,[25,33,34]

$$E_\omega = k_B T \ln\left(\frac{\omega_0}{\omega}\right). \qquad (6)$$

Traps below this demarcation can change their state and contribute, while those above cannot. Through the formalism of Walter et al., a tDOS profile can then be found through the differential,[10,21,25]

$$N_T(E_\omega) = -\frac{V_{bi}}{qW}\frac{dC}{d\omega}\frac{\omega}{k_B T}. \qquad (7)$$

Note, again only those states crossing the quasiFermi-level efficiently contribute and, in the low frequency limit, only those states between the Fermi-level and mid-gap will be probed.[25] The Walter formalism is highlighted in Fig. 1(b), where the known P3HT deep-trap profile is reproduced.[21] It is not until frequencies greater than 1 MHz that a significant portion of this deep-defect band is frozen and not responding. Thus, in the CV data of Fig. 1(a), as the frequency is swept higher, Eqs. (1) and (2) measured N decreases from $p + N_T$ to approach p as the traps are progressively excluded—explaining the frequency dependence.

The second artifact seen in Fig. 1(a) is a change in the MS slope as per increasing reverse bias. Namely, at a given frequency between -5 and $+1$ V_{DC} a straight line, as expected from the ideal MS treatment, is not noted. Instead, a rolling slope is clearly present. Simply, this could be caused by a non-uniform doping profile, as interpreted by Dennler et al.[18] However, as stated by Li et al., the change may also be due to the contribution of energetically deep defect states.[35] This interpretation of defect contribution can be derived from the capacitance model given by Kimmerling.[36] To summarize, consider CV data taken at a frequency which is faster than the trap emission time, but with a DC voltage sweep which is slower than the emission. The depletion edge is measured at W_d, but both mobile-holes and charges emitted from defects crossing the quasiFermi-level are collected.[36] For voltages that put the junction near flatband condition with little or no band bending, N then represents p.[36] However, as band-bending increases through reverse-bias, emitted trap-charge is included and $N = p + N_T$.[36] To quantify, this case has $\nu_{AC} > e_p > \nu_{\Delta VDC}$ and the N measured by Eqs. (1) and (2) then actually represents,

$$N(x) = N_T(x_T)\left[1 - \frac{W_d - x_T}{W_d}\right] + N_A(W), \qquad (8)$$

where x_T is the spatial demarcation where the trap energy, E_T, is within $k_B T$ of the Fermi-level and W_d-x_T is assumed to remain constant.[10,36] Clearly, when x_T is small, N indeed represents p. However, as x_T begins to dominate the depletion width, N(x) more closely represents $p + N_T$. Neglecting non-uniform doping [for the time being] and taking the Kimmerling interpretation, the reverse bias CV profile of Fig. 1(a) can be readily explained by the inclusion of the deep-defect profile shown in Fig 1(b).

Pushing further, a simple quantification gives an interesting revelation. Fig. 1(b) shows that at ca. $E_\nu = 0.46$ eV, or just below 1 kHz, the known deep-defect is fully responding. However, in the MS plot of Fig. 1(a), at frequencies <1 kHz the slope still gives some change in increasing reverse-bias. This seems to be representative of

yet unknown, deeper defects ($e_p < \nu_{AC}$) being pulled to the quasiFermi-level to contribute. This thought is developed in the subsequent sections using a more targeted application of the above-summarized CF and CV measurements.

III. DEEPER DEFECTS: IDENTIFICATION AND CHARACTERIZATION

A. Low frequency capacitance measurements

As an initial step towards identifying and characterizing this suspected distribution, we probe deeper into the energy-gap with low frequency capacitance measurements. The CF measurement is valid between the Fermi-level and mid-gap;[25,37] however, current CF data on P3HT:PCBM OPVs extend only to ca. 10 Hz (ca. 578 meV). Thus, we probe deeper towards the mid-gap with frequencies nearing 10 mHz (ca. 756 meV). Measurements at these frequencies proved difficult as the AC impedance becomes high and noise can dominate. To combat this, thicker devices (>200 nm) were used. Thicker films seem counterintuitive as the geometric impedance is actually increased. However, the longer drying times of thicker films give the phases more time to segregate across the vertical axis.[38] Thus, less shunt paths percolate, resulting in less leakage. Thicker devices have the added advantage of ensuring proper doping extraction from CV MS, which has recently been cautioned.[39] Fig. 2(a) shows the resulting CF data normalized to geometric capacitance.
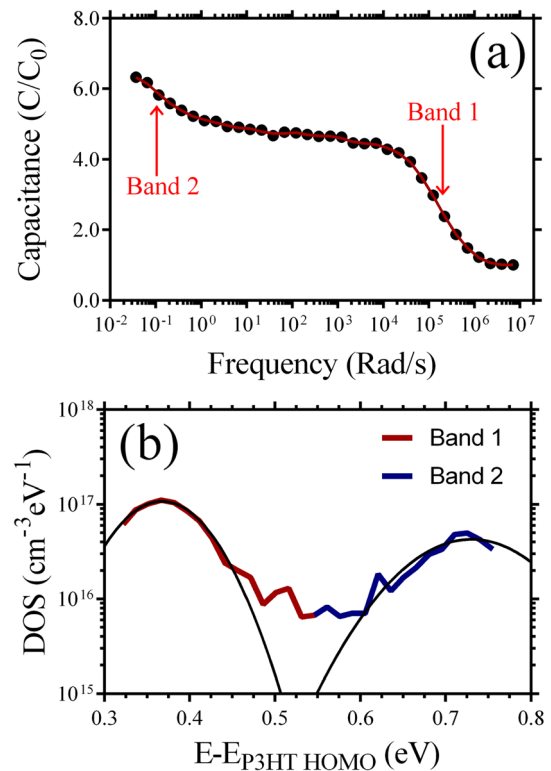

FIG. 2. (a) CF spectra normalized to geometric capacitance (ca. 1.10 nF) showing two dominate regions of increasing capacitance. Red, solid line shows polynomial fit. (b) Resulting tDOS energy spectra showing two Gaussian defect bands as per the Walter et al. model. Y-axis calculated via Eq. (7) and X-axis by Eq. (6).

TABLE I. Summary of calculated parameters from CF data; average ± SEM shown.

	Cohen and Lang model		Walter *et al.* model		
	L_D (nm)	N_T (cm^{-3})	N_T (cm^{-3})	E_0 (eV)	σ (meV)
Band 1	…	…	$1.70 \pm 0.40 \times 10^{16}$	0.33 ± 0.01	42.3 ± 3.30
Band 2	…	…	$0.60 \pm 0.20 \times 10^{16}$	0.69 ± 0.02	48.2 ± 8.50
Total	13.1 ± 2.30	$3.12 \pm 0.67 \times 10^{16}$	$2.30 \pm 0.60 \times 10^{16}$	…	…

Initial information can be obtained through the derivation from the model of Cohen and Lang. An estimation of the Debye length and concentration of measured trap states is given by Eqs. (4) and (5). These results are summarized in Table I; average ± standard error of the mean (SEM) for four representative devices is shown. The distribution can be further resolved using the model of Walter *et al.* Fig. 2(b) shows the energy spectra calculated by Eq. (7). Before solving, data were cleaned using a polynomial averaging (solid, red line in Fig. 2(a)). The resolved bands were then fit using a Gaussian form,

$$N_T(E_\nu) = \frac{N_T}{\sqrt{2\pi}\sigma} \exp\left[-\frac{(E_o - E_\nu)^2}{2\sigma^2}\right], \qquad (9)$$

where N_T is the concentration of traps, E_0 the mean energy, and σ the disorder parameter. The supplementary material contains repetitions and variations of this measurement and analysis.[48] Table I summarizes the parameter extraction; the average ± the SEM for four representative devices is shown.

Two distinct bands are seen in the resulting spectrum: one in the high (>1 kHz) frequencies and one in the low (<1 Hz) frequencies. The shallower, high-frequency band correlates well to the data presented in Fig. 1 and FTSC ($E_{oFTSC} = 0.35$ eV),[17] CF ($E_{oAS} = 0.36$–0.38 eV),[21,22] and Poole-Frenkel conduction modeling (PFCM) ($E_{oPFCM} = 0.30$–0.50 eV)[23] data presented in the literature. Any deviation in the mean energy stems from the choice of ν_o (see supplementary material),[48] while deviations in concentration result from the growth-rate dependence.[22] The deeper, low-frequency band represents a previously unknown defect distribution—as predicted by the above-discussed CV interpretation. This band has a mean energy of 0.69 eV above the highest occupied molecular orbital (HOMO), ca. 0.36 eV deeper in the gap than known band 1. Although this deeper band is smaller in amplitude, it is still on the order of 5×10^{16} cm^{-3} eV^{-1}, indicating it may play a significant role in altering OPV performance. This is especially true considering the deeper an energetic defect resides, the more strongly it can trap carriers. In a disordered material, trap states can contribute to current through thermally activated tunneling and hopping.[3] However, at sufficiently deep levels charge transfer is cut-off and the states are static.[3] The strongly trapped charge may then act as a monomolecular recombination center, a charged point site or both. Good agreement in the total concentration of measured traps between the two models is clearly seen. No significant statistical difference (p-value > 0.05) was found in the displayed averages.

B. High frequency point-by-point CV

In order to test if the newly discovered deep-defect distribution accounts for the slope change in the lower frequency CV data, one might intuitively measure the MS profile at <10 mHz in search of a straight plot. This experiment, however, was dominated by noise, making it difficult to ascertain meaningful results. Thus, we next turn to a point-by-point differential of high frequency CV measurements in an attempt to make correlations between Eq. (8) and the tDOS profile of Fig. 2(b).

CV data taken at 800 kHz from −5 to +1 V_{DC} are displayed in Fig. 3(a). The MS form shows the expected rolling slope. Equation (2) was used to generate the *depth* profile of Fig. 3(b), which we believe is best represented by the Kimmerling model of Eq. (8). To be thorough, Cohen and Lang have also described this dynamic DC response and their interpretation has already been employed within the organic community.[24,31] However, our data did not match with that described in the cited work and we found better applicability of the Kimmerling formalism. The highest possible frequency
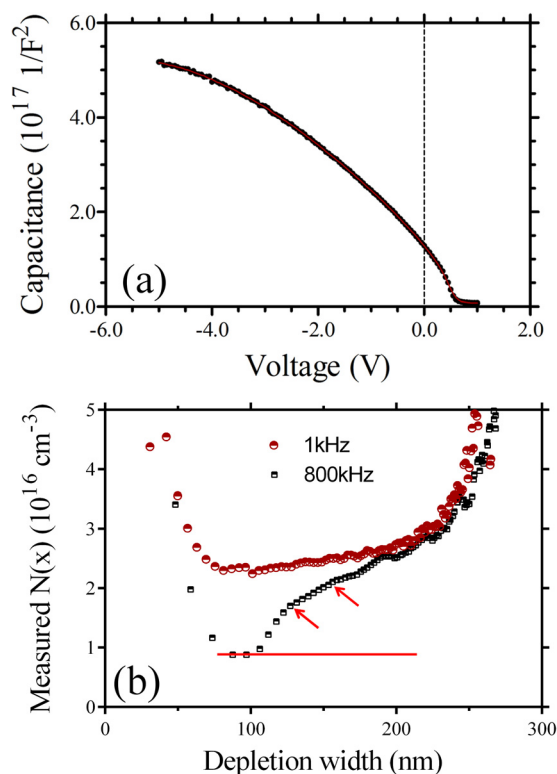

FIG. 3. (a) High frequency CV shown in Mott-Schottky form. Red, solid line shows polynomial fit. (b) Measured N(x) versus W for CV of (a) as solved by Eq. (2).

before complete freeze out was used to ensure case 2 of the Kimmerling theory was invoked and that $\langle x \rangle = W_d$.[10,36]

In Fig. 3(b) (800 kHz), a decrease followed by a minimum and gradual increase in N(x) is seen. The minimum point corresponds to a voltage very near V_{bi}, where the bands are nearly flat and, because a high frequency was employed, only p responds. At higher forward-bias, the depletion width reduces, carriers are injected, and a chemical capacitance begins to dominate.[39–41] At increasing reverse-bias, the depletion width is increased, bands are bent, and the possible contributions of trap states are seen.

To begin, let us neglect the possibility of a non-uniform doping profile and consider the Gaussian defects of Fig. 2(b) as they are pulled to the quasiFermi-level to contribute to the CV measurement. Starting from near the flat-band condition, a sharp increase in N(x) would first be seen with increasing reverse bias. As the Gaussian center is passed, defect states are still included, but at a slower rate, causing an inflection in N(x). As the next Gaussian is pulled, a second inflection would be found, and so on. In Fig. 3(b), red arrows highlight those inflections which we expect correspond to dominate Gaussian distributions. By subtracting the values of N(x) at the inflections to the left and right of a suspected distribution, the total defects of that band is found. Assuming homogeneous doping, these values should correlate to those found by CF, while deviations may be indicative of a non-uniform doping profile. Indeed, we find good agreement between the magnitude of the CV distributions (Fig. 3(b), red arrows) and the CF (Fig. 2(b)) defect bands. For this particular cell, CV gave the band 1 concentration to be 8.81×10^{15} cm^{-3} and band 2 to be 3.67×10^{15} cm^{-3}. This compares to CF values of 9.12×10^{15} cm^{-3} (high frequency band) and 3.07×10^{15} cm^{-3} (low frequency band) respectfully. Further, a lower frequency (1 kHz) analysis is also included in Fig. 3(b). At 1 kHz, the first defect distribution is already responding and, in accordance with the above theory, the profile is pivoting upwards. The trend will limit towards a straight line (i.e., with a low enough measurement frequency), which represents the mobile charges plus total defect states.[10] The pivot and expected straight-line limit can be seen near 2.7×10^{16} cm^{-3} in this particular device. The difference between the 1 kHz profile and straight limit is about 3–4×10^{15} cm^{-3}, the value of the low-frequency, deeper distribution not yet included in low-bias 1 kHz measurement. This again supports the existence of a distribution deeper in the gap and, because the depth profile of inhomogeneous doping would be independent of frequency, further rules out the possibility of non-uniform doping. The supplementary material shows the reproducibility and variation of this measurement.[48]

C. Polymer only diode and dark current modeling

To give indication as to the spatial location of these defects, a set of experiments were conducted to repeat the above measurements again on 1:1 P3HT:PCBM OPVs as well as 1:0 P3HT only diodes with both Al and Ca/Al cathodes. Table II summarizes the results, average ± standard error of the mean, for three representative sets. Unpaired t-tests showed no significant statistical differences (p-value > 0.05) in

TABLE II. Summary of tDOS characteristic parameters for 1:1 and 1:0 devices.

	A (cm^{-3} eV^{-1})	E$_o$ (eV)	σ (meV)
1:1 band 1	$18.0 \pm 2.50 \times 10^{16}$	0.31 ± 0.004	40.3 ± 3.50
1:0 band 1	$15.0 \pm 2.80 \times 10^{16}$	0.32 ± 0.005	33.3 ± 1.10
1:1 band 2	$3.10 \pm 0.30 \times 10^{16}$	0.66 ± 0.003	41.1 ± 7.40
1:0 band 2	$3.30 \pm 0.40 \times 10^{16}$	0.65 ± 0.007	44.7 ± 1.60

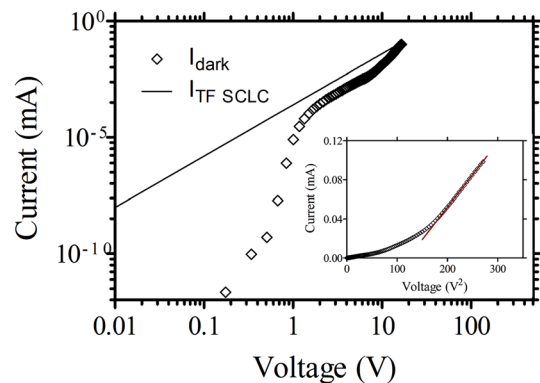|	p (cm^{-3})	N$_T$ capacitance (cm^{-3})	N$_T$ dark IV (cm^{-3})
1:1	$3.30 \pm 1.20 \times 10^{16}$	$4.90 \pm 1.10 \times 10^{16}$	n/a
1:0	$2.30 \pm 0.84 \times 10^{16}$	$4.00 \pm 1.30 \times 10^{16}$	$4.70 \pm 0.53 \times 10^{16}$

FIG. 4. Dark current versus voltage for P3HT diode. The solid line represents the trap-free model ($\mu = 2 \times 10^{-4}$ cm^2/V s). The inset shows dark current versus voltage squared.

any 1:1 to 1:0 parameter comparison. This, coupled with data showing no difference in trap parameters between devices with an Al cathode and those with a Ca/Al cathode, strongly indicates the measured levels are belonging to the polymer bulk. Further, because of the prominent decrease in the MS slope with deeper reverse bias (i.e., increase in measured N), we expect the traps to be acceptor-like.[42]

As seen in Table II, dark-current modeling measurements were also conducted to generally verify the capacitance results. The dark current of a basic polymer diode is often described as space charge limited.[14,43,44] Fig. 4 shows the dark IV of a representative indium tin oxide (ITO)/P3HT/Al diode. In the ln-ln plot, three main regions prevail: (i) ohmic in low voltages, (ii) trap controlled in intermediate voltages, and (iii) trap free at high voltages.[14,43] The high voltage region is governed by $J_{TF} = 9/8 \epsilon \mu V^2 / L^3$ (solid line in Fig. 4), where J α V^2 (Fig. 4 inset).[14] By examining the voltage at which current switches from trap controlled to trap free (V_{TF}), the total defect states can be estimated by $N_T = 2 \epsilon_s V_{TFL} / (qL^2)$.[45] The concentration estimated by dark IV agrees well with that determined via capacitance, substantiating the general capacitance measurement.

IV. CONCLUSION

Further elucidations into the capacitive behavior of P3HT:PCBM based photovoltaic cells were presented. A

background of CV/CF analysis was given and evidence indicating the presence of a yet unknown deep-defect distribution was highlighted. Low frequency CF measurements were then undertaken to identify and characterize this deep band. The model of Cohen and Lang was used to determine the Debye length as well as the measured trap concentration. The formalism of Walter *et al.* gave good corroboration to the total concentration and further resolved the tDOS energy spectrum—directly revealing the presence of the predicted distribution. This new defect was then reproduced using the Kimmerling interpretation of high-frequency CV measurements. Good correlation between CV and CF data confirms the presence of the deep defect and, especially when coupled with dark-current modeling data, shows no spatial variations in the doping profile. A comparison of PCBM containing devices to that of polymer only diodes with different cathodes strongly indicates the measured defects to be acceptor-like traps belonging to the polymer bulk. The findings presented here are important for the understanding and optimization of organic solar cells and we suspect the presented methods to be generally applicable to other OPV material sets.

V. EXPERIMENTAL

OPV cells were fabricated from P3HT (Reike Metals, 50 k MW, 90%–94% regioregularity, $<0.04\%$ Ni/$<0.02\%$ Zn/$<0.04\%$ Br) and PCBM (NANO C, Inc.). Bulk heterojunction mixtures of 1:1 or 1:0 by weight (20–30 mg/ml) P3HT:PCBM were mixed with ortho-dichlorobenzene (Sigma-Aldrich) and stirred at $45\,^\circ$C for at least 12 h. ITO (Delta Technologies) substrates were treated by consecutive sonications in: (i) isopropyl/acetone (50:50 v/v), (ii) detergent/deionized water, (iii) ethanol/methanol (50:50 v/v), and (iv) deionized water. The substrates were then blown dry and treated with air plasma. A ca. 30 nm poly(ethylenedioxythiophene): poly(styrenesulfonic acid) (HC Stark) film was spin-coated onto the treated substrates and the casted films were annealed at $120\,^\circ$C for 10 min. The blend solutions were then filtered via plastic-syringe (note, this is known to affect the solution's wettability)[46] and a $0.22\,\mu$m PTFE filter (Sigma-Aldrich). The active layer was then spun at 400 to 600 rpm for 60 s onto the PEDOT covered substrates and slow-dried in a Petri dish. Lastly, a ca. 1500 Å thick Al cathode was thermally evaporated at a rate of <5 Å/s under a 10^{-6} mbar vacuum.

Capacitance measurements were taken using a PARSTAT 2273 in the dark, at room temperature and in open air. Four averages per data-point and a 3 s delay between successive measurements were used to increase data-quality. A small-signal amplitude of 10 to 25 mV (rms) was used for linearity and the impedance magnitude ($|Z|$) was monitored to ensure proper model employment.[47] CF data were taken at a 0 V DC bias. To rule out oxygen induced artifacts during the longer low frequency measurements, a set of measurements were also conducted in nitrogen atmosphere—no differences were found. Further, the measurements were always conducted as CV, CF, and repeat CV in order to ensure no differences in the oxygen induced doping were seen during the data collection time.

[1] Z. He, C. Zhong, S. Su, M. Xu, H. Wu, and Y. Cao, Nature Photon. **6**(9), 593–597 (2012).
[2] T. Kirchartz, K. Taretto, and U. Rau, J. Phys. Chem. C **113**(41), 17958–17966 (2009).
[3] L. Kaake, P. Barbara, and X. Y. Zhu, J. Phys. Chem. Lett. **1**(3), 628–635 (2010).
[4] B. A. Gregg, J. Phys. Chem. C **113**(15), 5899–5901 (2009).
[5] B. A. Gregg, Soft Matter **5**(16), 2985–2989 (2009).
[6] M. Mandoc, F. Kooistra, J. Hummelen, B. de Boer, and P. Blom, Appl. Phys. Lett. **91**, 263505 (2007).
[7] R. A. Street and M. Schoendorf, Phys. Rev. B **81**(20), 205307 (2010).
[8] C. Deibel and A. Wagenpfahl, Phys. Rev. B **82**(20), 207301 (2010).
[9] R. Street, Phys. Rev. B **82**(20), 207302 (2010).
[10] J. Heath and P. Zabierowski, "Capacitance spectroscopy of thin-film solar cells," in *Advanced Characterization Techniques for Thin Film Solar Cells* (Wiley-VCH, 2011), pp. 81–105.
[11] G. Garcia-Belmonte, P. P. Boix, J. Bisquert, M. Lenes, H. J. Bolink, A. La Rosa, S. Filippone, and N. Martín, J. Phys. Chem. Lett. **1**, 2566 (2010).
[12] M. S. A. Abdou, F. P. Orfino, Y. Son, and S. Holdcroft, J. Am. Chem. Soc. **119**(19), 4518–4524 (1997).
[13] L. Goris, A. Poruba, L. Hodakova, M. Vanecek, K. Haenen, M. Nesladek, P. Wagner, D. Vanderzande, L. De Schepper, and J. Manca, Appl. Phys. Lett. **88**(5), 052113 (2006).
[14] V. Nikitenko, H. Heil, and H. Von Seggern, J. Appl. Phys. **94**, 2480 (2003).
[15] J. Schafferhans, A. Baumann, C. Deibel, and V. Dyakonov, Appl. Phys. Lett. **93**, 093303 (2008).
[16] J. Schafferhans, A. Baumann, A. Wagenpfahl, C. Deibel, and V. Dyakonov, Org. Electron. **11**(10), 1693–1700 (2010).
[17] P. Yu, A. Migan-Dubois, J. Alvarez, A. Darga, V. Vissac, D. Mencaraglia, Y. Zhou, and M. Krueger, J. Non-Cryst. Solids **358**, 2537–2540 (2012).
[18] G. Dennler, C. Lungenschmied, N. S. Sariciftci, R. Schwödiauer, S. Bauer, and H. Reiss, Appl. Phys. Lett. **87**, 163501 (2005).
[19] S. Neugebauer, J. Rauh, C. Deibel, and V. Dyakonov, Appl. Phys. Lett. **100**(26), 263304 (2012).
[20] D. Q. Feng, A. Caruso, Y. B. Losovyj, D. Shulz, and P. Dowben, Polym. Eng. Sci. **47**(9), 1359–1364 (2007).
[21] P. P. Boix, G. Garcia-Belmonte, U. Munecas, M. Neophytou, C. Waldauf, and R. Pacios, Appl. Phys. Lett. **95**(23), 233302–233303 (2009).
[22] K. S. Nalwa, R. C. Mahadevapuram, and S. Chaudhary, Appl. Phys. Lett. **98**, 093306 (2011).
[23] C.-Y. Nam, D. Su, and C. T. Black, Adv. Funct. Mater. **19**(22), 3552–3559 (2009).
[24] J. D. Cohen and D. V. Lang, Phys. Rev. B **25**(8), 5321 (1982).
[25] T. Walter, R. Herberholz, C. Muller, and H. Schock, J. Appl. Phys. **80**(8), 4411–4420 (1996).
[26] B. G. Streetman and S. Banerjee, *Solid State Electronic Devices* (Prentice-Hall, 1995).
[27] S. Hoshino, M. Yoshida, S. Uemura, T. Kodzasa, N. Takada, T. Kamata, and K. Yase, J. Appl. Phys. **95**, 5088 (2004).
[28] M. Glatthaar, N. Mingirulli, B. Zimmermann, T. Ziegler, R. Kern, M. Niggemann, A. Hinsch, and A. Gombert, Phys. Status Solidi A **202**(11), R125–R127 (2005).
[29] G. Garcia-Belmonte, A. Munar, E. M. Barea, J. Bisquert, I. Ugarte, and R. Pacios, Org. Electron. **9**(5), 847–851 (2008).
[30] V. Dyakonov, I. Riedel, C. Deibel, J. Parisi, C. Brabec, N. Sariciftci, and J. Hummelen, in 2001 MRS Spring Meeting - Symposium C – Electronic, Optical and Optoelectronic Polymers and Oligomers (Mater. Res. Soc. Symp. Proc., 2002).
[31] D. Ray and K. Narasimhan, J. Appl. Phys. **103**(9), 093711–093716 (2008).
[32] D. Mencaraglia, S. Ould Saad, and Z. Djebbour, Thin Solid Films **431–432**, 135–142 (2003).
[33] F. Reis, L. Santos, R. Bianchi, H. Cunha, D. Mencaraglia, and R. Faria, Appl. Phys. A: Mater. Sci. Process. **96**(4), 909–914 (2009).
[34] S. S. Hegedus and E. Fagen, J. Appl. Phys. **71**(12), 5941–5951 (1992).

[35]J. V. Li, A. M. Nardes, Z. Liang, S. E. Shaheen, B. A. Gregg, and D. H. Levi, Org. Electron. **12**(11), 1879–1885 (2011).

[36]L. Kimerling, J. Appl. Phys. **45**(4), 1839–1845 (1974).

[37]P. Würfel and U. Würfel, *Physics of Solar Cells* (Wiley Online Library, 2005).

[38]M. Campoy-Quiles, T. Ferenczi, T. Agostinelli, P. G. Etchegoin, Y. Kim, T. D. Anthopoulos, P. N. Stavrinou, D. D. C. Bradley, and J. Nelson, Nature Mater. **7**(2), 158–164 (2008).

[39]T. Kirchartz, W. Gong, S. A. Hawks, T. Agostinelli, R. C. I. MacKenzie, Y. Yang, and J. Nelson, J. Phys. Chem. C **116**(14), 7672 (2012).

[40]K. Harada, A. Werner, M. Pfeiffer, C. Bloom, C. Elliott, and K. Leo, Phys. Rev. Lett. **94**(3), 36601 (2005).

[41]A. Sharma, P. Kumar, B. Singh, S. R. Chaudhuri, and S. Ghosh, Appl. Phys. Lett. **99**, 023301 (2011).

[42]A. Campbell, D. Bradley, E. Werner, and W. Brütting, Synth. Met. **111**, 273–276 (2000).

[43]T. P. Nguyen, Phys. Status Solidi A **205**(1), 162–166 (2008).

[44]V. Kumar, S. Jain, A. Kapoor, J. Poortmans, and R. Mertens, J. Appl. Phys. **94**, 1283 (2003).

[45]K. C. Kao, *Dielectric Phenomena in Solids* (Academic Press, 2004).

[46]J. A. Carr, K. S. Nalwa, R. Mahadevapuram, Y. Chen, J. Anderegg, and S. Chaudhary, ACS Appl. Mater. Interfaces **4**(6), 2831–2835 (2012).

[47]J. A. Carr and S. Chaudhary, Appl. Phys. Lett. **100**(21), 213902–213904 (2012).

[48]See supplementary material at http://dx.doi.org/10.1063/1.4818324 for supporting data and details.

On the identification of deeper defect levels in organic photovoltaic devices

John A. Carr[a] and Sumit Chaudhary[a,b]
[a]*Department of Electrical and Computer Engineering, Iowa State University, Ames, Iowa 50011, USA*
[b]*Department of Materials Science Engineering, Iowa State University, Ames, Iowa 50011, USA*

Supplementary material

Photovoltaic Performance

Illuminated J-V data was generated a AM1.5 using an ELH quartzline lamp at 1 sun. The system was calibrated using a crystalline silicon photodiode coupled with a KG-5 filter. STable I summarizes the photovoltaic performance plotted in SFig. 1.

V_{oc} (V)	J_{sc} (mA/cm^2)	FF (%)	PCE (%)
0.543 ± 0.01	10.90 ± 0.20	55.80 ± 2.80	3.30 ± 0.20

STable I: Summary of photovoltaic performance parameters.
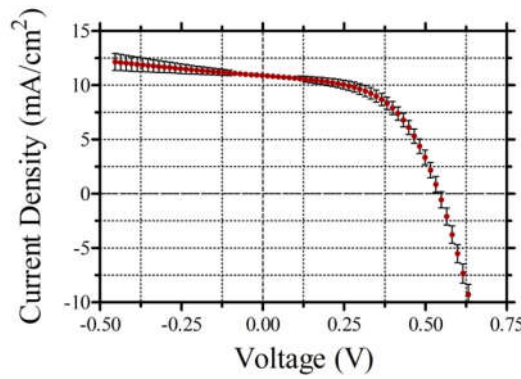
SFig. 1. Photovoltaic performance of the studied P3HT:PCBM BHJ cells.

Attempt-to-escape frequency

ν_o, the attempt-to-escape frequency, is a characteristic parameter which represents the prefactor of trap emission. It is especially important for finding the exact depth of the measured defect-bands in the Water *et al.* model. Previous admittance spectroscopy reports have used a ν_o of 10^{12}-10^{13} s^{-1} as an estimation stemming from inorganic materials.[1, 2] However, a more recent report has called this value into question, citing an attempt to escape frequency of 33.42 s^{-1}.[3] The first (10^{12} -10^{13} s^{-1}) is slightly higher than and the latter (210 rad/s) significantly lower than values of 10^7-10^9 s^{-1}, which have been extracted from poly(*p*-phenylene vinylene (PPV) based organic cells.[3-6] To comment on this, we use information from the freeze out frequencies and doping levels of our devices.

First, we examine high frequency CF (Fig. 2a in main article). It can be seen that, for this particular device, at *ca.* 800kHz the freeze out condition is reached – which corresponds to the demarcation energy of Eq. 6 (in the main article) reaching the Fermi-level. Freeze out frequencies ranging from 800kHz to 1.5MHz were seen in our devices. Next, we use high frequency CV with Mott-Schottky analysis to find the density of mobile charges and solve for E_F – $E_{P3HT\ Valance}$ by sEq. 1.

$$E_F - E_{P3HT\ HOMO} = k_B T \ln\left(\frac{N_V}{p}\right) \qquad (s1)$$

Values for N_v ranging from 10^{19} to 10^{21} cm^{-3} have been used in the literature.[7-9] Thus, we approximate v_o to be between 1x10^9 and 5x10^{10} s^{-1} depending on the choice of N_v. In this report, we choose $N_v = 10^{21}$ cm^{-3} as it seems to be most commonly employed, giving $v_o = 5x10^{10}$ s^{-1}.

A more accurate treatment of the attempt to escape frequency is given by sEq. 2,[10]

$$v_o = \beta_p N_V \tag{s2}$$

where β_p is the capture coefficient of the trap. Note that the parameter is dependent on temperature as well as the characteristics of the trap being probed.[11] Thus, we acknowledge more in-depth work is needed to find the exact attempt to escape frequency(ies). In the meantime, we expect the above to give a reasonable estimate for the work at hand.

Low Frequency CF Repetitions

To highlight reproducibility and variation, the following shows repetitions for the CF measurement reported in the primary manuscript. Eq. 7 was used to solve for the DOS versus energy spectra shown below.
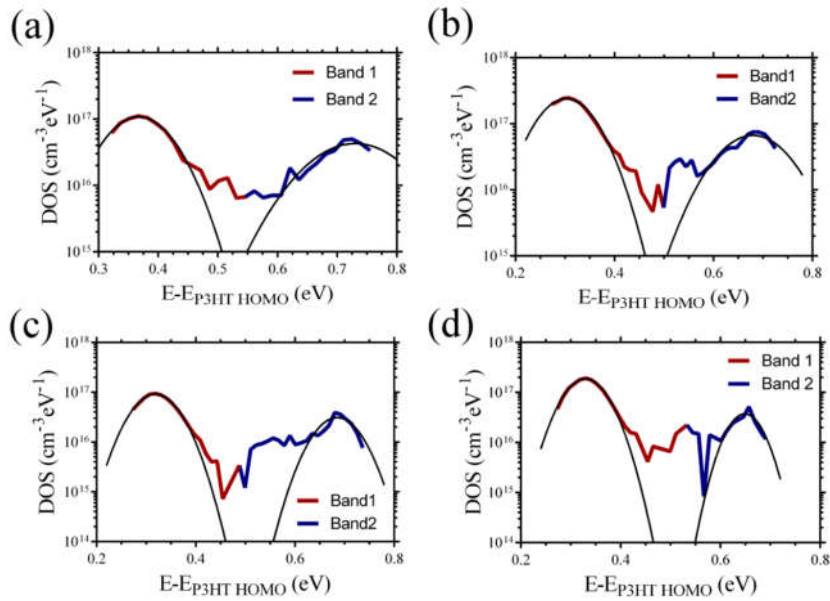
SFig. 2. Repeats of low-frequency CF measurements. The DOS spectra after solving Eq. 7 (primary article) are shown. The parameters of IDs (a)-(d) are summarized in STable II.

Each device showed the distinct presence of two deep-defect bands, one in high frequencies and one in low frequencies. STable II summarizes the Gaussian fit parameters for each band. Thickness values were obtained by geometric capacitance measurements – the devices were depleted by a large reverse DC bias ($\geq$ -5 VDC) and a high frequency ($\geq$ 500 kHz) was used to ensure only a dielectric response.

ID	Thickness (nm)	Band	A (cm^{-3} eV^{-1})	E$_0$ (eV)	σ (meV)
(a)	300	1	10.8 x10^{16}	0.36	47.5
		2	2.99 x10^{16}	0.73	41.0
(b)	204	1	24.0 x10^{16}	0.30	48.2
		2	6.70 x10^{16}	0.68	60.0
(c)	266	1	9.20 x10^{16}	0.32	38.5
		2	3.00 x10^{16}	0.68	41.0
(d)	235	1	18.8 x10^{16}	0.33	35.2
		2	3.80 x10^{16}	0.65	27.6

STable II: Summary of Gaussian fit parameters for the tDOS plots of SFig. 2.

Point-by-point CV Repetitions

Repeats for the high frequency CV measurement shown in Fig. 3 of the primary manuscript are displayed in SFig. 3. For each ID (a)-(d) the raw CV data is displayed in the left column, while the profiles, as calculated by Eq. 2 of the primary file, are shown on the right. STable 3 summarizes the trap concentrations.
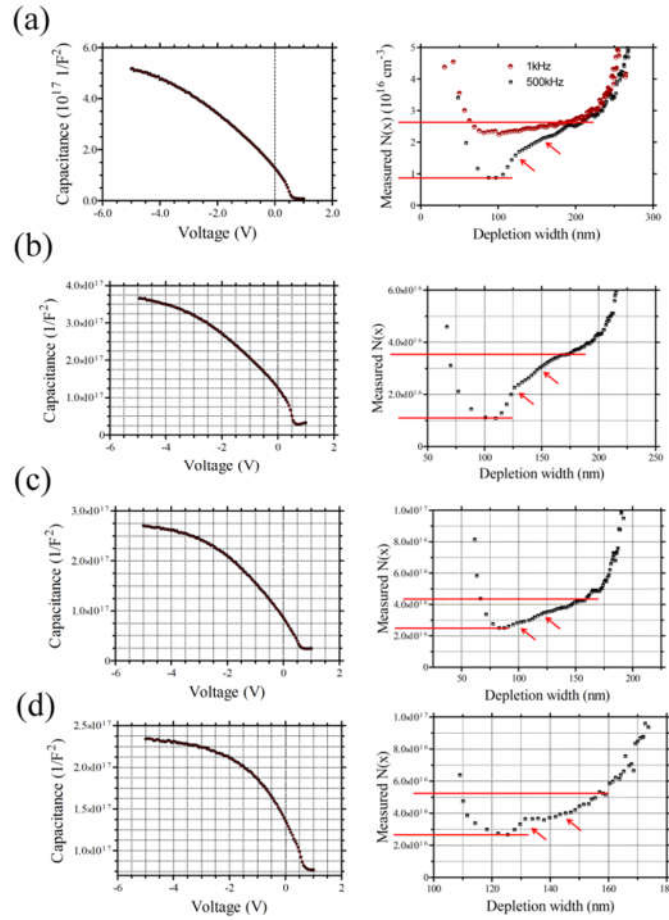
SFig. 3. Repeats of high-frequency CV analysis from +1 to -5 V$_{DC}$. CV data (left column) was solved by Eq.2 of the primary article to give the profile on the right.

ID	Frequency (kHz)	Band	N_T (cm^{-3})
(a)	800	1	8.80×10^{15}
		2	3.10×10^{15}
(b)	700	1	1.50×10^{16}
		2	8.00×10^{15}
(c)	700	1	8.50×10^{15}
		2	5.90×10^{15}
(d)	500	1	1.40×10^{16}
		2	3.60×10^{15}

STable III: Summary of band amplitudes for CV profiles of IDs (a)-(d) shown in SFig. 3.

All calculated concentrations (STable III) are consistent with the representative data presented in the primary article.

References

1. P. P. Boix, G. Garcia-Belmonte, U. Munecas, M. Neophytou, C. Waldauf and R. Pacios, Applied Physics Letters **95** (23), 233302-233303 (2009).
2. K. S. Nalwa, R. C. Mahadevapuram and S. Chaudhary, Applied Physics Letters **98**, 093306 (2011).
3. P. P. Boix, J. Ajuria, I. Etxebarria, R. Pacios and G. Garcia-Belmonte, Thin Solid Films (2011).
4. V. Dyakonov, D. Godovsky, J. Meyer, J. Parisi, C. Brabec, N. Sariciftci and J. Hummelen, Synthetic metals **124** (1), 103-105 (2001).
5. V. Dyakonov, I. Riedel, C. Deibel, J. Parisi, C. Brabec, N. Sariciftci and J. Hummelen, presented at the MATERIALS RESEARCH SOCIETY SYMPOSIUM PROCEEDINGS, 2002 (unpublished).
6. A. Campbell, D. Bradley, E. Werner and W. Brütting, Synthetic metals **111**, 273-276 (2000).
7. R. C. I. MacKenzie, C. G. Shuttle, M. L. Chabinyc and J. Nelson, Advanced Energy Materials (2012).
8. C. Tanase, E. Meijer, P. Blom and D. De Leeuw, Physical Review Letters **91** (21), 216601 (2003).
9. J. Nolasco, R. Cabre, J. Ferré-Borrull, L. Marsal, M. Estrada and J. Pallares, Journal of applied physics **107** (4), 044505-044505-044504 (2010).
10. T. Walter, R. Herberholz, C. Muller and H. Schock, Journal of applied physics **80** (8), 4411-4420 (1996).
11. J. Heath and P. Zabierowski, Advanced Characterization Techniques for Thin Film Solar Cells, 81-105 (2011).